Hybrid-kinetic simulations of Alfvén-wave interruption

J. Squire[1,2]† and M. Kunz[3,4] and E. Quataert[5] and A. A. Schekochihin[6,7]

[1]Theoretical Astrophysics, 350-17, California Institute of Technology, Pasadena, CA 91125, USA

[2]Walter Burke Institute for Theoretical Physics

[3]Department of Astrophysical Sciences, Princeton University, 4 Ivy Lane, Princeton, New Jersey 08544, USA

[4]Princeton Plasma Physics Laboratory, PO Box 451, Princeton, NJ 08543, USA

[5]Astronomy Department and Theoretical Astrophysics Center, University of California, Berkeley, CA 94720, USA

[6]The Rudolf Peierls Centre for Theoretical Physics, University of Oxford, 1 Keble Road, Oxford, OX1 3NP, UK

[7]Merton College, Oxford OX1 4JD, UK

(Received xx; revised xx; accepted xx)

Using two-dimensional hybrid-kinetic simulations, we explore the nonlinear "interruption" of standing and traveling shear-Alfvén waves in collisionless plasmas. Interruption involves a self-generated pressure anisotropy removing the restoring force of a linearly polarized Alfvénic perturbation, and occurs for wave amplitudes $\delta B_\perp/B_0 \gtrsim \beta^{-1/2}$ (where β is the ratio of thermal to magnetic pressure). We use highly elongated domains to obtain maximal scale separation between the wave and the ion gyroscale. We find that the dynamics of both standing and traveling waves are strongly affected by the excitation of oblique firehose modes, which decay into long-lived parallel fluctuations at the ion gyroscale that cause significant particle scattering. These parallel fluctuations are shown to arise generically through the free decay of oblique firehose fluctuations as the plasma becomes firehose stable, and survive over very long time periods due to a nonlinear stabilization of the cyclotron damping mechanism. Our results demonstrate that collisionless plasmas cannot support linearly polarized Alfvén waves above the amplitude $\delta B_\perp/B_0 \sim \beta^{-1/2}$. They also provide a vivid illustration of two key aspects of low-collisionality plasma dynamics: (i) the importance of velocity space instabilities in regulating plasma dynamics at high β, and (ii) how nonlinear collisionless processes can transfer mechanical energy directly from the largest scales into thermal energy and microscale fluctuations, without requiring a scale-by-scale turbulent cascade.

1. Introduction

Shear-Alfvén fluctuations are fundamenal to magnetized plasma dynamics (Alfvén 1942; Cramer 2011; Ogilvie 2016). They are routinely observed in laboratory plasmas (Gekelman *et al.* 2011), and are ubiquitous in the solar wind above the ion gyroscale (Bruno & Carbone 2013). As the basis for modern theories of magnetohydrodynamic (MHD) turbulence (Goldreich & Sridhar 1995; Boldyrev 2006; Schekochihin *et al.* 2009; Mallet & Schekochihin 2017), their physics plays a crucial role in the transfer of energy

† Email address for correspondence: jsquire@caltech.edu

from large to small scales, and they underlie some core differences between neutral and magnetized fluid dynamics. Shear-Alfvén waves are also the most robust plasma oscillation: linearly, they are weakly damped by kinetic effects in collisionless regimes (Foote & Kulsrud 1979) and survive in both kinetic and fluid plasma models (Cramer 2011).

In these proceedings, we study, using hybrid-kinetic simulations, a notable exception to this robustness, which was first examined in Squire *et al.* (2016). In a collisionless plasma, a linearly polarized shear-Alfvén (SA) wave above the amplitude

$$\frac{\delta B_\perp}{B_0} \gtrsim \beta^{-1/2}, \tag{1.1}$$

is strongly nonlinearly modified, or "interrupted." In Eq. (1.1), $\beta \equiv 8\pi p_0/B^2$ is the ratio of thermal pressure (p_0) to magnetic pressure (B is the field strength), B_0 is a background magnetic field, and $\delta B_\perp$ is an Alfvénically polarized field perturbation. In this work, we explore the fate of standing and traveling SA waves above the interruption limit (1.1). We find that such waves dissipate rapidly (in approximately one Alfvén time or less), heating the plasma and creating microscale fluctuations without developing into a turbulent cascade. These results are relevant to variety of astrophysical environments with hot, low-density, high-β plasmas; for example, the intracluster medium (Sparke & Gallagher 2007; Kunz *et al.* 2010; Zhuravleva *et al.* 2014), low-luminosity black-hole accretion flows (Quataert 1998; Yuan & Narayan 2014; Kunz *et al.* 2016), and large-scale fluctuations in the solar wind (Bale *et al.* 2009; Bruno & Carbone 2013; Chen 2016).

1.1. *Shear-Alfvén wave interruption*

Before continuing, let us briefly explain the origin of the limit (1.1) (see Squire *et al.* 2017 for details). The effect depends on the generation of pressure anisotropy, viz., a pressure tensor that differs in the directions perpendicular and parallel to the magnetic field (we denote these $p_\perp$ and $p_\parallel$, respectively). In a magnetized weakly collisional plasma where the collision frequency ν_c is less than the ion gyrofrequency Ω_i, a pressure anisotropy develops whenever the magnetic field strength changes in time. This anisotropy, $\Delta p \equiv p_\perp - p_\parallel$, causes an additional stress in the momentum equation $\nabla \cdot (\Delta p/B^2 \boldsymbol{BB})$, and if $\beta > 1$, the anisotropic stress can be as important as, or even dominate over, the magnetic tension $\nabla \cdot (\boldsymbol{BB})/4\pi = \boldsymbol{B} \cdot \nabla \boldsymbol{B}/4\pi$. This suggests that collisionless dynamics can differ significantly from MHD predictions, even for perturbations on large spatial ($\lambda \gg \rho_i$) or temporal ($\tau \gg \Omega_i^{-1}$) scales (here ρ_i is the ion gyroradius). Further, if Δp grows too large in either the positive or negative direction, the plasma becomes unstable to to fast-growing microinstabilities, which grow and saturate on scales approaching ρ_i. For $\beta > 1$ the most important of these are the firehose instability, which plays a prominent role in this work and is unstable for $\Delta p \lesssim -B^2/4\pi$ (Rosenbluth 1956; Chandrasekhar *et al.* 1958; Parker 1958; Yoon *et al.* 1993), and the mirror instability, which is unstable for positive anisotropies $\Delta p \gtrsim B^2/8\pi$.

Consider now the fate of an Alfvénic magnetic perturbation, with a large enough amplitude such that as the magnetic field decreases due to the Lorentz force, it generates a pressure anisotropy that is sufficiently large to destabilize the firehose instability. At this point, $\Delta p = -B^2/4\pi$, the anisotropic stress exactly offsets the Lorentz force, which is the restoring force for the wave. The development of the wave is thus "interrupted"—a nonlinear effect that is not captured in linear models of SA waves. Because the wave perturbs the field magnitude by $\delta B_\perp^2$, a wave amplitude above the limit (1.1) is sufficient to generate such a Δp in a collisionless plasma with $\nu_c \ll \omega_A \ll \Omega_i$ (where ω_A is the Alfvén frequency). Similarly, in the weakly collisional (Braginskii) regime (Braginskii

1965), where $\omega_A \ll \nu_c \ll \Omega_i$ and collisions balance the generation of pressure anisotropy, SA waves of amplitude

$$\frac{\delta B_\perp}{B_0} \gtrsim \sqrt{\frac{\nu_c}{\omega_A}}\beta^{-1/2}, \tag{1.2}$$

are interrupted and unable to oscillate. Although we will not explicitly add particle collisions in this work, the limit (1.2) is relevant when SA wave dynamics are influenced by scattering from microscale fluctuations.

1.2. *The purpose and organization of this article*

The purpose of these proceedings is to explore SA-wave interruption in a collisionless plasma, using the simplest model that might be expected to provide a qualitatively accurate representation of reality: hybrid kinetics (kinetic ions, fluid electrons) in two spatial and three velocity dimensions. The use of two spatial dimensions is necessary to correctly capture the oblique firehose instability (Yoon *et al.* 1993; Hellinger & Matsumoto 2000), even though we study long-wavelength standing and traveling SA waves that vary only in the field-parallel direction. We focus on maximizing the scale separation between the large-scale SA wave and the ion gyroscale, a limit that is relevant to many astrophysical environments. This setup is designed to address the role of finite-Larmor-radius (FLR) effects and particle scattering from microscale fluctuations after the nonlinear interruption of the wave. More generally, our results highlight the importance of microinstabilities in controlling large-scale dynamics in high-β weakly collisional plasmas.

The remainder of the article is organized as follows. In §2 we explain the hybrid method and detail the initial conditions and numerical parameters used for our simulations. We also explain (in §2.2.1 and §2.2.2) our reasons for focusing primarily on the case of a standing wave initialized with an Alfvénic magnetic perturbation. Then, in §3 and §4, we explore the dynamics of standing waves and traveling waves respectively, in each case explaining the observed large-scale dynamics based on simple arguments in previous works (Squire *et al.* 2017) and measurements of the particle scattering rate. In all our simulations, we see that particle scattering is dominated by short-wavelength parallel fluctuations ($k_\perp \sim 0$, $k_\| \rho_i \sim 1$) that evolve from oblique firehose modes §5 is devoted to examining the creation and evolution of these fluctuations in simplified settings, with an eye towards the eventual goal of constructing a theory for how microscale fluctuations influence the large-scale dynamics in different scenarios. We finish with conclusions and discussion in §6. For the reader with little time (for example, a conference attendee with an imposing collection of other papers to get through), §2.2, §3 and 3.1, and §6 give a flavor of the study and its key results.

2. Numerical method and simulation setup

In this section, we describe the hybrid-kinetic method and the *Pegasus* code, which is used for all simulations presented here. We then explain our numerical setup and the motivation for using this (§2.2.1 and §2.2.2), and briefly describe numerical tests used to ensure simulation accuracy (we give a fuller description of these tests in App. A).

2.1. *Hybrid-kinetic simulation*

The hybrid-kinetic approximation involves treating the electrons as an isothermal, massless, neutralizing fluid. By removing, light waves, plasma oscillations, and electron kinetic scales from the problem, the hybrid method reduces simulation cost dramatically, while still retaining fully kinetic ion dynamics. The hybrid approximation may be motivated—or derived, in the limit of collisional electrons—using a mass-ratio expansion, viz., an expansion in $(m_e/m_i)^{1/2} \approx 1/42$) (see, e.g., App. A of Rosin *et al.* 2011). The method may also be extended to include more complex electron physics (see, e.g., Cheng *et al.* (2013)), but we do not consider this here.

The hybrid equations consist of (i) the collisionless Vlasov equation for the ion distribution function $f_i(\boldsymbol{x}, \boldsymbol{v}, t)$,

$$\frac{\partial f_i}{\partial t} + \boldsymbol{v} \cdot \frac{\partial f_i}{\partial \boldsymbol{x}} + \frac{q_i}{m_i} \left(\boldsymbol{E} + \frac{1}{c} \boldsymbol{v} \times \boldsymbol{B} \right) \cdot \frac{\partial f_i}{\partial \boldsymbol{v}} = 0; \tag{2.1}$$

(ii) Faraday's law for the magnetic field,

$$\frac{\partial \boldsymbol{B}}{\partial t} = -c \nabla \times \boldsymbol{E}; \tag{2.2}$$

and (iii), a generalized Ohm's law for the electric field,

$$\boldsymbol{E} + \frac{1}{c} \boldsymbol{u}_i \times \boldsymbol{B} - \frac{\eta}{c} \nabla \times \boldsymbol{B} = -\frac{T_e \nabla n_i}{e n_i} + \frac{(\nabla \times \boldsymbol{B}) \times \boldsymbol{B}}{4\pi q_i n_i}. \tag{2.3}$$

In Eqs. (2.1)–(2.3), q_i and m_i are the ion's charge and mass, $\boldsymbol{E}$ is the electric field, c is the speed of light, η is the plasma resistivity, and T_e is the electron temperature (this is an arbitrary parameter within the hybrid model). The ion density n_i and bulk velocity $\boldsymbol{u}_i$ specified as moments of f_i,

$$n_i(\boldsymbol{x}, t) = \int d\boldsymbol{v} f_i(\boldsymbol{x}, \boldsymbol{v}, t), \tag{2.4}$$

and bulk flow velocity

$$u_i(\boldsymbol{x}, t) = \int d\boldsymbol{v}\, \boldsymbol{v} f_i(\boldsymbol{x}, \boldsymbol{v}, t), \tag{2.5}$$

thus closing the system.

We use the *Pegasus* code (Kunz *et al.* 2014*b*) to solve Eqs. (2.1)-(2.3). *Pegasus* employs the particle-in-cell (PIC) method to evolve the ion distribution function and constrained transport (Evans & Hawley 1988) to maintain $\nabla \cdot \boldsymbol{B} = 0$. Second-order particle shape functions are used for particle deposits (Birdsall & Langdon 1991), along with a predictor-corrector time integrator based on the Boris algorithm Boris (1970). We use the δf method (Chen & Parker 2003), which evolves only perturbations to the ion distribution function, $\delta f = f - f_0$, where f_0 is a reference distribution, which we take to be an isotropic Maxwellian. The method reduces discrete-particle noise by $\sim (\delta f / f_0)^2$. This makes it highly beneficial for simulation of high-β plasmas, where it is necessary to resolve very small ($\ll 1/\beta$) deviations from a Maxwellian distribution.

2.2. *Simulation setup*

Our simulation setup is designed to probe SA wave interruption under the simplest possible conditions. Accordingly, in these proceedings, focus on two specific initial conditions, which have variation only on scales very large compared to the ion gyroradius ($\lambda_A \gg \rho_i$, where λ_A is the SA wavelength). These are (i) a parallel standing SA wave, initialized with an out-of-plane magnetic perturbation, viz., initial conditions

$$\frac{\delta B_z}{B_0} = -\delta b \cos\left(\frac{2\pi}{\lambda_A} x \right), \quad \delta u_z = 0; \tag{2.6}$$

and (ii) a traveling SA wave, viz., initial conditions

$$\frac{\delta B_z}{B_0} = -\delta b \cos\left(\frac{2\pi}{\lambda_A}x\right), \quad \frac{\delta u_z}{v_A} = \delta b\, \cos\left(\frac{2\pi}{\lambda_A}x\right). \tag{2.7}$$

Here δb is the wave amplitude, λ_A is the wavelength, and the 2-D spatial domain spans the x and y dimensions. We focus on the SA standing wave in this work, for reasons discussed below (§2.2.1). Due to the larger computational domains required, we leave study of the important case of an initial Alfvénic velocity perturbation to future work (see §2.2.2 for further discussion).

In all simulations, we initialize using an isotropic Maxwellian ion distribution with $T_e = T_i$, and set $\eta = 0$.† We impose a background magnetic field $\boldsymbol{B} = B_0\hat{\boldsymbol{x}}$, with $\beta_i = 8\pi n_i T_i/B_0^2$. Each domain is of width $50\rho_i$ in the y direction and highly elongated (up to $L_x = 1000\rho_i$) in the x direction (with $\lambda_A = L_x$), so as to enable maximal scale separation between the SA wave and the oblique firehose instability (which produces perturbations with $k\rho_i \sim 0.5$). We use a spatial resolution of $\mathit{\Delta} x = 0.3125\rho_i$ and $N_{\rm ppc} =$ 4096 particles per cell (ppc). We take $\beta_i = 100$ and $\delta b = 0.5$, which is well above the interruption limit $\delta b_{\max} \approx 2\beta^{-1/2}$ (Squire *et al.* 2016). Within the MHD model, the initial conditions (2.6) or (2.7) with these parameters would create continuing sinusoidal SA oscillations (deviations due to compressibility are very small because $\beta \gg 1$; see Squire *et al.* 2017). For future reference, the SA wave period and gyrofrequency are related by $\tau_A = 2\pi/\omega_A = \sqrt{\beta_i}(\lambda_A/\rho_i)\mathit{\Omega}_i^{-1}$. Throughout the text we shall use angle brackets $\langle\cdot\rangle$ to denote a spatial average, and $\langle\cdot\rangle_y$ to denote an average across the perpendicular, in-plane direction (y). We will also use a tilde (e.g., $\delta\tilde{\boldsymbol{B}}$) to heuristically indicate that a quantity varies on the microscales (i.e., with $k\rho_i \sim 1$).

Due to the very large separation of space and time scales involved in this problem, careful numerical tests are important to ensure confidence in the observed results. In addition to previous tests of the *Pegasus* code (Kunz *et al.* 2014*b*), we have run a variety of low-amplitude wave tests and scaling studies that specifically concern the evolution of long-wavelength SA waves. These are detailed in App. A. Most importantly, these tests indicate that a SA wave below the limit (1.1) can propagate/oscillate normally in *Pegasus*, for the same numerical parameters used for the nonlinear SA wave simulations.

2.2.1. *Standing waves and traveling waves*

Throughout this work, we focus primarily on the SA standing wave, as opposed to the traveling wave. Our reason for this choice is that the types of physical effects seen in standing SA waves are more likely to be generally applicable to Alfvénic turbulence (although both setups are of course highly idealized). In particular, the standing wave is relevant to SA waves where a large-scale $dB/dt \neq 0$ causes a large region of the plasma to become firehose unstable at once, while the traveling wave setup specifically probes initial conditions where $\langle dB/dt\rangle = 0$ initially, and the wave must be damped (by Landau damping and pressure anisotropy damping; Hollweg 1971; Squire *et al.* 2017) before reaching the firehose limit. Thus a "mixed" SA wave, which is both traveling and oscillating, or a wave with a range of wavelengths, will be better described by the standing-wave phenomenology so long there is a globally oscillating component of $\delta B_\perp$ that causes $\mathit{\Delta} p$ to reach the firehose limit. It thus seems likely that the dynamics of the standing wave are more generically relevant to Alfvénic turbulence. In any case, once the $\mathit{\Delta} p$ has reached the firehose limit, we shall see that the dynamics of standing and

† In the hot, low density plasmas of interest, the resistivity due to electron-ion collisions is very small.

traveling SA waves are broadly similar, with similar sources particle scattering that cause the large-scale SA wave to decay.

2.2.2. *Initial Alfvénic velocity perturbation*

The present study has an important omission—a standing SA wave initialized with a velocity perturbation. Such initial conditions are likely very relevant for Alfvénic turbulence, since it is hard to envisage how an isolated Alfvénic magnetic perturbation (e.g., initial conditions (2.6)) might arise, if not through a velocity perturbation of some sort. It is, however, reasonable to expect that such a fluctuation should behave similarly to the initial magnetic perturbation studied here. In particular, even though $\Delta p > 0$ initially, the mirror instability grows when $\Delta p \gtrsim B^2/8\pi$ and acts to limit Δp (Schekochihin *et al.* 2008; Rincon *et al.* 2015; Melville *et al.* 2016; Squire *et al.* 2017), likely allowing Δp to decrease and reach the firehose limit ($\Delta p \lesssim B^2/4\pi$) after magnetic tension reverses dB/dt as the SA wave oscillates. However, kinetic simulations are certainly needed to address this physically relevant situation more confidently. We have delayed these studies to future work for computational reasons: the mirror instability depends more significantly on scale separation ($\lambda_A/\rho_i \gg 1$) than the firehose instability (Kunz *et al.* 2014*a*), and even larger simulation domains will be required.

2.2.3. *The oblique and parallel firehose instabilities*

The standard firehose instability threshold quoted above, $\Delta p = -B^2/4\pi$, is only truly valid in the long-wavelength limit (the "MHD firehose"). As is well documented for $\beta \sim 1$ in a bi-Maxwellian plasma (e.g., Hellinger & Matsumoto 2000; Klein & Howes 2015), kinetic effects and resonances shift the instability boundary to $\Delta p > -B^2/4\pi$ for small-scale modes ($k\rho_i \sim 1$). So far as we are aware, there is no detailed study of the $\beta \gg 1$ limit, but preliminary investigations (not shown) have indicated that the oblique firehose instability can be unstable at $\Delta p > -B^2/4\pi$ when $\beta \gg 1$.† The parallel firehose instability is slower growing (due to its larger scale) and is only unstable for $\Delta p \leqslant -B^2/4\pi$ when $\beta \gg 1$ (Schekochihin *et al.* 2010). For simplicity, throughout this work, we shall base our discussion on the long-wavelength parallel firehose threshold, because of its key importance for long-wavelength SA wave dynamics. Issues relating to the behavior of oblique firehose modes at $\Delta p > -B^2/4\pi$ will be considered in more detail in future work.

3. Standing shear-Alfvén wave

In this section, we discuss the evolution of standing SA waves. The discussion is centered around our largest simulation, with scale separation $\lambda_A/\rho_i = 1000$ and initial condition (2.6). We describe the evolution of the large-scale δB_z, δu_z, and Δp, and how this is related to the detailed evolution of the oblique firehose modes that are initially excited. We then discuss how the wave heats the plasma in §3.1, and the scaling of SA wave behavior with $\lambda_A/\rho_i = 1000$ in §3.2.

Figure 1 shows the spatiotemporal evolution of the out-of-plane magnetic perturbation δB_z for the SA standing wave with $\lambda_A/\rho_i = 1000$. It is helpful, for the sake of discussion, to divide the evolution of the wave into four distinct phases of nonlinear evolution. These are:

† The character of the instability changes at the long-wavelength threshold $\Delta p = -B^2/4\pi$, and it appears to be less effective at suppressing the growth of pressure anisotropy when $\Delta p > -B^2/4\pi$. This observation heuristically agrees with previous studies at lower β (e.g., Hellinger & Trávníček 2008), and solar wind observations (Chen *et al.* 2016).

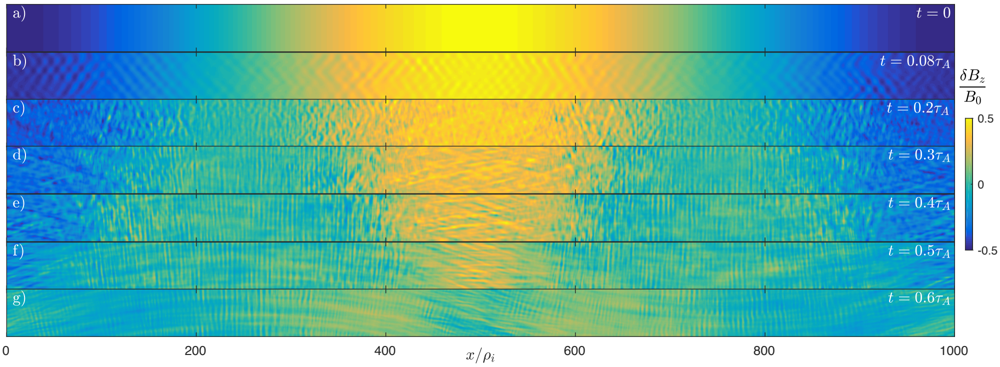

FIGURE 1. The evolution of $\delta B_z(x,t)$ in a SA standing wave with $\lambda_A/\rho_i = 1000$, $\tau_A = 10000\Omega_i^{-1}$. Following the decrease in B due to the Lorentz force ($t = 0$; panel (a)), which causes $\Delta p < -B^2/4\pi$, the wave erupts into oblique firehose modes ($t = 0.08\tau_A$; panel(b)). In the least unstable regions around the wave nodes (where $4\pi\Delta p/B^2 \approx -0.7$), the oblique firehose modes transition into $k_\| \rho_i \sim 1$ Alfvénic fluctuations that scatter particles (these are visible from $t/\tau_A \approx 0.2$ onwards). This causes the large-scale SA wave to decay (panels (c)–(f)) by $t/\tau_A \approx 0.6$ (panel (g)) in a manner that closely resembles SA wave dynamics in the Braginskii regime.

(i) The initial field decrease, which occurs between $t = 0$ and $t/\tau_A \approx 0.08$. At the end of this phase, the changing B has created a negative anisotropy $\Delta p < -B^2/4\pi$ that is large enough to nullify the magnetic tension and trigger the firehose instability.

(ii) The eruption of oblique firehose modes (Yoon *et al.* 1993; Hellinger & Matsumoto 2000; see Fig. 1(b)), which push the plasma back above $\Delta p > -B^2/4\pi$ due to the fast-growing small-scale magnetic field perturbations (Schekochihin *et al.* 2008; Rosin *et al.* 2011; Kunz *et al.* 2014*a*).

(iii) The transition of the oblique firehose modes into parallel ($k_\perp \sim 0$), small-scale ($k_\| \rho_i \sim 1$) Alfvénic fluctuations, which scatter particles at a relatively high rate and allow the wave to decay (Fig. 1(c)–(f)).

(iv) The dissolution of the large-scale SA wave into low-amplitude (but still large-scale) SA waves, which can oscillate freely without causing the plasma to reach the firehose limit (Fig. 1(g))

Out of these stages, (iii) provides a crucial point of difference compared to the predictions of 1-D Landau-fluid (LF) models (Snyder *et al.* 1997; Squire *et al.* 2016; Squire *et al.* 2017). In particular, the high particle scattering rate, which occurs due to the $k_\| \rho_i \sim 1$ Alfvénic modes that evolve from decaying oblique firehose modes, causes fast decay of the large-scale SA wave in a manner that strongly resembles waves in the weakly collisional Braginskii regime (Braginskii 1965; Squire *et al.* 2017). We now explain the physics of these stages in more detail, focusing in particular on the consequences of particle scattering in stage (iii).

Initial field decrease and interruption: stages (i) and (ii).

A more quantitative illustration of the wave decay process is given in Figs. 2 and 3, which show the 1-D (y-averaged) wave profiles and the magnetic-energy spectrum, respectively. The initial sinusoidal δB_z is shown with the black line in Fig. 2(a), along with $\delta u_z/v_A$ (blue dot-dashed line) and the firehose parameter $4\pi\Delta p/B^2$ (red line), which is -1 at the parallel firehose instability threshold. As magnetic tension causes δB_z (and thus B) to decrease, Δp decreases also, reaching the firehose limit at $t \approx 0.07\tau_A$ when $\langle \delta B_z(\boldsymbol{x}, t=0)^2 - \delta B_z(\boldsymbol{x}, t)^2 \rangle / B_0^2 \approx 4/3\beta^{-1}$ (Squire *et al.* 2017). Because $\delta B_z/B_0 = 0.5 > \beta^{-1/2}$, the plasma reaches the firehose instability threshold with only a

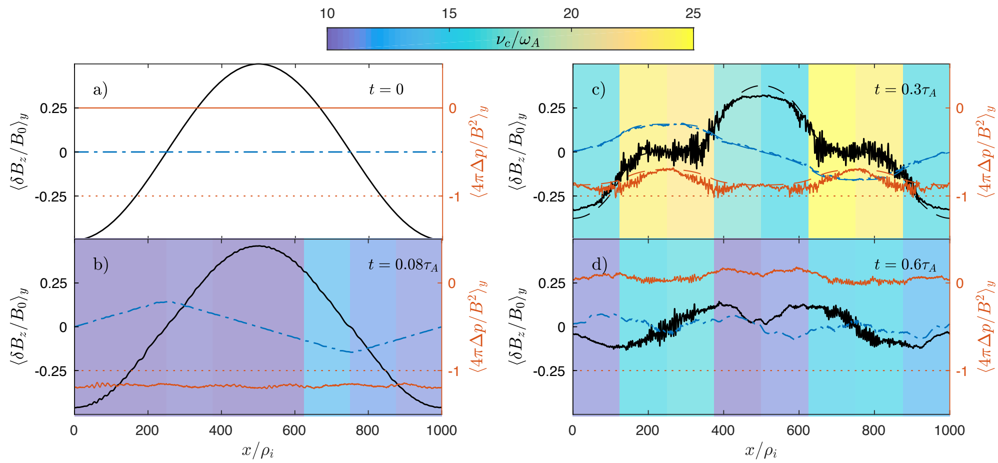

FIGURE 2. Evolution of the standing wave from Fig. 1. Each panel shows the y-averaged magnetic perturbation $\delta B_z/B_0$ (black line, left-hand axis), $\delta u_z/v_A$ (blue dot-dashed line, left-hand axis), and firehose parameter $4\pi\Delta p/B^2$ (red, right-hand axis; the dotted line shows the parallel firehose instability threshold), for some of the times illustrated in Fig. 1. In panels (b)-(d), the background color (see top for color scale) illustrates the collisionality ν_c/ω_A caused by particle scattering from microscale fluctuations, measured over the time intervals $t/\tau_A \in [0.07, 0.15]$ (panel (b)), $t/\tau_A \in [0.2, 0.4]$ (panel (c)), and $t/\tau_A \in [0.55, 0.65]$ (panel (d)). In panel (c) we additionally show (with dashed lines) $\delta B_z/B_0$, $\delta u_z/v_A$ (this is almost identical to the simulation result and hard to see), and $4\pi\Delta p/B^2$ for a decaying SA standing wave in the Braginskii model at $\beta = 100$, $\nu_c/\omega_A \approx 10$, and $t/\tau_A = 0.3$, illustrating the qualitative similarity to the collisionless dynamics.

small ($\sim$%3) change in δB_z (Fig. 2(b)). During this process, heat fluxes rapidly smooth pressure perturbations along field lines (Squire *et al.* 2017), causing $\Delta p(\boldsymbol{x}, t)$ to be nearly homogeneous in space (Fig. 2(b)) and leading to the sudden eruption of oblique firehose modes (Yoon *et al.* 1993; Hellinger & Matsumoto 2000; Kunz *et al.* 2014*a*) across the entire wave at once (see Fig. 1(b)). At this point, with $4\pi\Delta p \approx -B^2$, the large-scale wave has no restoring force because magnetic tension is exactly nullified by the pressure-anisotropic stress. However, with B now *increasing* due to the fast-growing firehose modes, Δp is quickly (by $t \approx 0.085\tau_A$) pushed back above $\Delta p > -B^2/4\pi$, where it stays for the remainder of the wave's evolution.

Towards the end of stage (ii), the evolution of the oblique firehose modes (now in a plasma with $\Delta p > -B^2/4\pi$) is key for the subsequent large-scale SA wave dynamics. If these modes evolve to scatter particles sufficiently fast, over sufficiently long time periods, δB_z can decay with the anisotropy at or near $\Delta p = -B^2/4\pi$; if they do not (e.g., if they decay quickly due to transit-time damping†), δB_z will be unable to decrease, as suggested by LF calculations (Squire *et al.* 2016). Because the anisotropy varies across the wave, and strongly influences the firehose dynamics, it is helpful to conceptually split the wave into two regions: the first around the wave nodes where there is no velocity shear $S = |\nabla \boldsymbol{u}|$ and $\delta B_z \approx 0$, the second around the wave antinodes where $S \sim \beta^{-1/2}\omega_A \approx 6 \times 10^{-5}\Omega_i$ ‡ and $\delta B_z \approx \delta B_z(t = 0)$. In the wave node region, the anisotropy is not driven by a large-scale dB/dt and the firehoses freely decay¶ (Quest & Shapiro 1996; Seough *et al.* 2015;

† Linearly, small-scale oblique modes $k_\perp\rho_i \gtrsim k_\parallel\rho_i \sim 1$ are strongly transit-time damped in a high-β plasmas; see Foote & Kulsrud (1979); Quataert (1998); Gary (2004).

‡ This estimate arises from solution of the wave equation for the amplitude of the $k = 2\pi/\lambda_A$ SA wave mode, $\partial_t^2 \delta b = -v_A^2(\delta b + (3/8)\beta(\delta b^2 - \delta b(0)^2)$ (Squire *et al.* 2017), at the time that $\Delta = -2/\beta$ (see Fig. 2(b)).

¶ In fact, the anisotropy at the nodes is being driven (to some degree) by the heat fluxes,

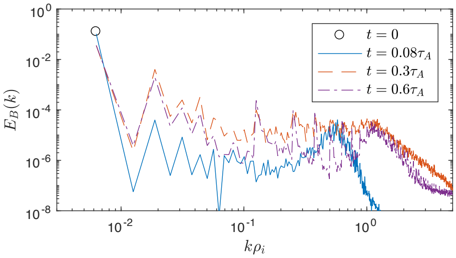

FIGURE 3. Energy spectrum of the magnetic field in the standing SA wave, at the times shown in Fig. 2 (Fig. 1(a), (b), (d), and (g)). The shift of firehose modes to smaller scales as they decay above the firehose limit is very clear if we compare the spectrum at $t = 0.08\tau_A$ with those at $t = 0.3\tau_A$ and $t = 0.6\tau_A$. The strong fluctuations at $k\rho_i \sim 1$ at these later times are responsible for the fast decay of the large-scale wave.

Melville *et al.* 2016) from early in their secular growth phase (Schekochihin *et al.* 2008). In the antinode regions, the situation, at least initially, is more similar to a continuously driven anisotropy (Matteini *et al.* 2006; Hellinger & Trávníček 2008; Kunz *et al.* 2014*a*; Melville *et al.* 2016; Riquelme *et al.* 2016) due to the shear flow set up by the initial decay of the wave (see $\delta u_z/v_A$ in Fig. 2(b), for $x/\rho_i \in [250, 750]$).

Large-scale SA wave decay: stages (iii) and (iv).

It appears—at least for the values of λ_A/ρ_i accessible so far—that it is the nodes of the wave that cause the strongest particle scattering and allow the wave to decay. This is surprising, given that these regions of space are the *least* firehose unstable, with $4\pi\Delta p/B^2 \approx -0.7$ throughout the decay (see, e.g., Fig. 2(c)). The cause for this behavior is a strong preference for firehose modes to decay into parallel Alfvnic modes. These modes, which can be seen clearly from $t/\tau_A = 0.2$ to $t/\tau_A = 0.6$ in Fig. 1, as well as in a comparison of the magnetic spectra between $t/\tau_A = 0.08$ and $t/\tau_A > 0.3$ in Fig. 3, are efficient particle scatterers due to their small scale $k_\parallel\rho_i \sim 1$ (compared to oblique firehose modes, which grow at $k\rho_i \sim 0.5$; see Fig. 3). This scattering is illustrated directly by the background color scale in Fig. 2, which shows the effective ion collisionality ν_c/ω_A as a function of space (this is measured by tracking sample ions; see App. B). We see that during the initial excitation of oblique firehose modes (from $t/\tau_A = 0.07$ to 0.15; Fig. 2(b)), the scattering is relatively weak (the modest variation in space here is simply noise due to the small time bin used for this phase). However, by $t = 0.3\tau_A$, the scattering is stronger and concentrated at the wave nodes, where the firehose modes have already decayed into parallel fluctuations. The parallel modes evolve and decay very slowly, as can be seen by their presence at the wave nodes in Fig. 1 throughout the wave decay ($t/\tau_A \geqslant 0.2$; see also Fig. 3), as well as the relatively high collisionality even after the large-scale δB_z has decayed (Fig. 2(d)). More discussion of these parallel modes—why they occur, and why they survive over such long time periods—is given in §5.

Surprisingly, the oblique firehose fluctuations at the wave antinodes contribute much less to the scattering, even though they are continuously driven by the shear $S \sim \beta^{-1/2}\omega_A$ throughout the decay. Measurements and scalings in Melville *et al.* (2016) suggest that such a shear should create secularly growing fluctuations that saturate and scatter particles at an amplitude $\langle(\delta\tilde{\boldsymbol{B}}/B_0)^2\rangle \sim (S\beta/\Omega_i)^{1/2} \sim 0.08$ after a timescale $t \sim (\Omega_i\beta/S)^{1/2}\Omega_i^{-1} \sim 1250\Omega_i^{-1} = 0.125\tau_A$. It appears that this scenario does not

so the oblique firehose mode do not strictly decay freely. To our knowledge, anisotropy driving through heat fluxes has not been studied in previous literature.

occur because the anisotropy driving at the antinodes, $d\Delta p/dt \sim -|S|p_0$, is balanced by scattering from parallel modes at the SA wave nodes (through the heat fluxes), rather than the secular growth of small-scale fluctuations at the antinodes. This illustrates the interesting nonlocality of high-β collisionless dynamics, which arises to the high thermal speed of ions, $v_{\mathrm{th},i} \sim \beta^{1/2}v_A$ (i.e., the heat fluxes; Squire *et al.* 2017). Evidently, care must be taken when applying results obtained in homogenous settings (e.g., Kunz *et al.* 2014*a*; Melville *et al.* 2016) to situations where plasma parameters (e.g., Δp or B) vary in space.

With this known source of particle scattering, the subsequent evolution of the large-scale SA wave is relatively easily understood: because $\omega_A \ll \nu_c \ll \Omega_i$, the plasma is in a regime that resembles the Braginskii collisional limit (Braginskii 1965) and the SA wave behaves as discussed in Squire *et al.* (2017), Sec. 4.1. We illustrate the qualitative similarity to Braginskii dynamics in Fig. 2(c), which also shows δB_z, δu_z, and $4\pi\Delta p/B^2$ (dashed lines) for a Braginskii wave at $\beta = 100$ $\nu_c \approx 10$.† We include heat fluxes in the Braginskii model, as appropriate at these parameters (more specifically, we solve Eq. (B15) of Squire *et al.* 2017). The "humped" shape of the SA wave occurs because the plasma must maintain $dB/dt < 0$ in order to overcome isotropization by collisions and stay at the firehose threshold. This causes the perturbation to split into regions where $4\pi\Delta p \approx -B^2$ and $d\delta B_z/dt < 0$ (around the antinodes), and regions where $4\pi\Delta p > -B^2$ and $\delta B_z = 0$ (these spread outwards from the nodes; see Fig. 1(c)–(f)). The wave decay time t_{decay} is determined by ν_c (through $\omega_A t_{\mathrm{decay}} \sim \beta(\delta B_\perp/B_0)^2/(\nu_c/\omega_A)$), because ν_c controls the relationship between Δp and dB/dt (specifically $\Delta p \approx \nu_c^{-1}p_0B^{-1}dB/dt$; Squire *et al.* 2017). In the simulation of Fig. 1, the ν_c that arises through scattering from microscale flucations is sufficiently large that the wave decays within one Alfvén time, viz., the wave is approximately at the Braginskii interruption limit (1.2), with $\nu_c/\omega_A \sim \beta(\delta B_\perp/B_0)^2$ (Squire *et al.* 2017). Note, however, that this does not imply that the wave is well-described by the Braginskii model all through its evolution: scattering from microscale fluctuations occurs only *after* the excitation of firehose instabilities, so any wave above the collisionless interruption limit (1.1) will be nonlinearly modified (i.e., the Braginskii model is relevant only after interruption).

Finally, it is worth noting that the wave decay generates a δB_y perturbation (this can be seen in Fig. 1 for $t/\tau_A \gtrsim 0.4$). Unfortunately, at the scale separations (λ_A/ρ_i) currently accessible, it is unclear whether this effect is appreciably stronger than the δB_y generation that occurs in a linear standing SA wave due to FLR effects.

3.1. *Plasma heating*

As the large-scale SA wave decays, it heats the plasma. This process does not involve a turbulent cascade, but rather a direct transfer of large-scale mechanical energy,

$$E_{\mathrm{mech}} = \frac{1}{2}\int d\boldsymbol{x}\, m_i n_i \boldsymbol{u}_i^2 + \frac{1}{8\pi}\int d\boldsymbol{x}\, B^2, \tag{3.1}$$

into thermal energy,

$$E_{\mathrm{th}} = \frac{1}{2}\int d\boldsymbol{x} \sum_r \Pi_{rr}, \tag{3.2}$$

† Although this scattering rate is not identical to that measured in Fig. 2, it is close enough (within a factor of ~ 2) to be reasonable, given the vagaries involved in measuring ν_c(see App. B).

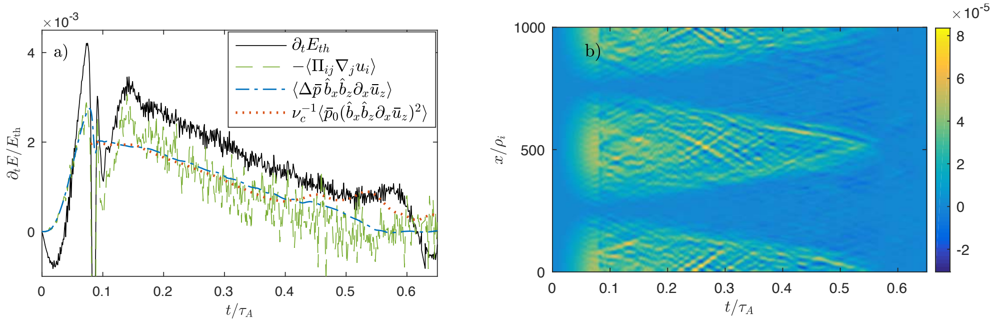

FIGURE 4. Plasma heating due to the standing wave in Fig. 1. In panel (a), we compare the rate of change of thermal energy $\partial_t E_{\rm th} = \int d\boldsymbol{x}\, n_i \sum_r \partial_t (\Pi_{rr}/n_i)/2$ (black line), with mechanical heating -$\int d\boldsymbol{x} \sum_{rs} \Pi_{rs} \nabla_r u_s$ (green dashed line), heating from the large-scale SA wave $\int d\boldsymbol{x}\, \Delta\bar{p}\, \hat{b}_x \hat{b}_z \partial_x \bar{u}_z$ (blue dot-dashed line; here $\bar{\cdot}$ denotes a filter that smooths fluctuations with $k\rho_i \gtrsim 0.25$), and the approximate viscous heating (Kunz *et al.* 2010) from the SA wave after interruption $\nu_c^{-1} \int d\boldsymbol{x}\, \bar{p}_\parallel (\hat{b}_x \hat{b}_z \partial_x \bar{u}_z)^2$ (red dotted line; we use $\nu_c/\omega_A \approx 10$ as in Fig. 2(c)).We normalize heating rates by $E_{\rm th}$ and use units of τ_A (note the small values, which is because $\beta \gg 1$). The initial $\partial_t E_{\rm th} < 0$ is due to the creation of $\boldsymbol{E}$ fluctuations in the (initially quiescent) plasma, due to particle noise (see App. A). In panel (b), we show how the heating is localized in space, as illustrated by $\int dy\, \Delta\bar{p}\, \hat{b}_x \hat{b}_z \partial_x \bar{u}_z$ (the color scale is in units of $E_{\rm th}/\tau_A/\rho_i$). As expected, the heating is localized around the wave antinodes, where the large-scale δB_z decays in time (c.f., Fig. 1(c)–(f)), and is approximately constant in space and time across the regions.

where Π_{rs} is the ion pressure tensor. Neglecting the creation of electric fields, this occurs through the heating term

$$\partial_t E_{\rm th} = -\int d\boldsymbol{x} \sum_{rs} \Pi_{rs} \nabla_r u_s \approx \int d\boldsymbol{x}\, \Delta p\, \hat{\boldsymbol{b}} \cdot (\hat{\boldsymbol{b}} \cdot \nabla \boldsymbol{u}) \approx \int d\boldsymbol{x}\, \Delta p\, \frac{d \ln B}{dt}, \tag{3.3}$$

where the last approximations assume gyrotropy and incompressibility. This heating is essentially the viscous dissipation of the wave. The rate, and total energy budget, are mediated by particle scattering from microscale fluctuations, because this enables $d \ln B/dt \neq 0$ (and $\Delta p \neq 0$) throughout the wave decay. The scattering also enables the thermalization of the energy and makes the process irreversible, returning the system to an approximately isotropic Maxwellian distribution by $t/\tau_A \approx 0.6$ (see Fig. 2(d)).

In Fig. 4(a), we compare the measured $\partial_t E_{\rm th}$ with heating due to the SA wave decay. Although the agreement is not perfect, due to spurious grid heating (see App. A.3 for discussion), we can clearly see the various stages of wave decay discussed above: during stage (i), the plasma is heated by the creation of pressure anisotropy (this heating is reversible); as the firehose fluctuations erupt in stage (ii) (at $t/\tau_A \approx 0.08$), there is a sudden drop in $\partial_t E_{\rm th}$ as the thermal energy of the plasma feeds into the oblique firehose instability; during stages (iii)–(iv), $\partial_t E_{\rm th} \gtrsim 0$ as $\delta B_\perp$ decays, which is due to the (irreversible) heating from the decay of the large-scale SA wave with $\Delta p \approx -B^2/4\pi$.

In addition to the basic comparison of heating with $\partial_t E_{\rm th}$, Fig. 4 also illustrates the heating that arises due to the large-scale SA wave only. This is done by computing the heating rate from $\partial_x u_z$ (i.e., the SA wave) only, after smoothing all fields over scales $k\rho_i \gtrsim 0.25$. Fig. 4 shows that the overall energetics are well captured by considering only these large-scale dynamics. We further show that this is well approximated (after the wave has interrupted) by a (parallel) viscous heating rate

$$(\partial_t E)_{\rm viscous} \approx \frac{p_0}{\nu_c} \int d\boldsymbol{x}\, (\hat{b}_x \hat{b}_z \partial_x u_z)^2 = \nu_{\rm Brag} \int d\boldsymbol{x}\, (\hat{b}_x \hat{b}_z \partial_x u_z)^2, \tag{3.4}$$

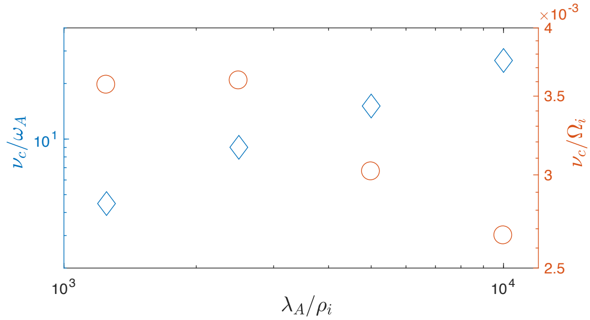

FIGURE 5. Scattering rate ν_c from microscale fluctuations excited by the SA wave, as a function of scale separation λ_A/ρ_i, for a suite of standing wave simulations (initial conditions (2.6)). In each case, the rate is measured using the technique described in App. B, across the entire domain $x \in [0, L_x]$, and over the time interval $t/\tau_A \in [0.1, 0.5]$, viz., from just after firehose excitation until the large-scale δB_z has mostly decayed (the results do not depend strongly on the exact choice of time interval). On the left-hand axis (blue diamonds), we normalize ν_c by ω_A; on the right-hand axis (red circles), we normalize by Ω_i. If the wave decay time $t_{\mathrm{decay}}/\tau_A$ is to become constant in the $\lambda_A/\rho_i \to \infty$ limit, ν_c/ω_A must tend to a constant value also.

with $\nu_c/\omega_A \approx 10$ as in Fig. 2(c), and ν_{Brag} the Braginskii "viscosity". The general agreement with the SA wave heating rate acts as a consistency check for the Braginskii comparison made in Fig. 2. In Fig. 4(b) we show how the SA wave heating is localized in space. During stage (iii), its local value is relatively constant in space and time, because the rate of field decrease (dB/dt) around the antinodes is approximately constant, so as to maintain a constant Δp. However, the spatial extent of the region being heated decreases in time as the antinode regions (where $dB/dt \neq 0$ and $\delta B_z \neq 0$) become smaller (c.f., Fig. 1(c)–(f)), causing the total heating rate (Fig. 4(a)) to decrease in time.

Overall, these results are promising for the development of closure models that approximate the effects of microinstabilities on large-scale dynamics without having to explicitly resolve the microscales.

3.2. *The importance of scale separation*

A natural question that arises from the discussion above is: how does the SA wave behave in the limit $\lambda/\rho_i \to \infty$? In addition to the $\lambda_A/\rho_i = 1000$ case discussed extensively above, we have also run a set of identical SA standing wave simulations at $\lambda_A/\rho_i = 500$, $\lambda_A/\rho_i = 250$, and $\lambda_A/\rho_i = 125$. These simulations have broadly similar dynamics to the $\lambda_A/\rho_i = 1000$ SA wave, although the micro- and macro-scale dynamics become confusingly intertwined for $\lambda_A/\rho_i \leqslant 250$.

However, it is clear from these simulations that we have not yet reached the true asymptotic limit, $\lambda/\rho_i \to \infty$. This is indicated by two observations:

(i) The scattering rate due to microscale fluctuations, averaged over the decay of the large-scale SA wave, is an increasing function of λ_A/ρ_i. Because $\omega_A t_{\mathrm{decay}} \propto (\nu_c/\omega_A)^{-1}$ this implies that the time required for the wave to decay is a decreasing function of λ_A/ρ_i, which is indeed the case.† The scaling of ν_c is shown quantitatively in Fig. 5, which plots the average ν_c over the wave's decay for each of the standing-wave simulations ($\lambda_A/\rho_i \in [125, 1000]$). The left and right axes in Fig. 5 show ν_c/ω_A and $\nu_c/\Omega_i = (\nu_c/\omega_A)(\lambda_A/\rho_i)^{-1}$ respectively, illustrating that while ν_c/ω_A increases with λ_A, ν_c/Ω_i decreases with λ_A

† For example, at $\lambda_A/\rho_i = 250$, the large-scale δB_z is completely decayed only after $t/\tau_A \approx 0.8$, while at $\lambda_A/\rho_i = 1000$ it decays by $t/\tau_A \approx 0.55$ (c.f., Figs. 2(c) and 11(b), which show intermediate times for each case).

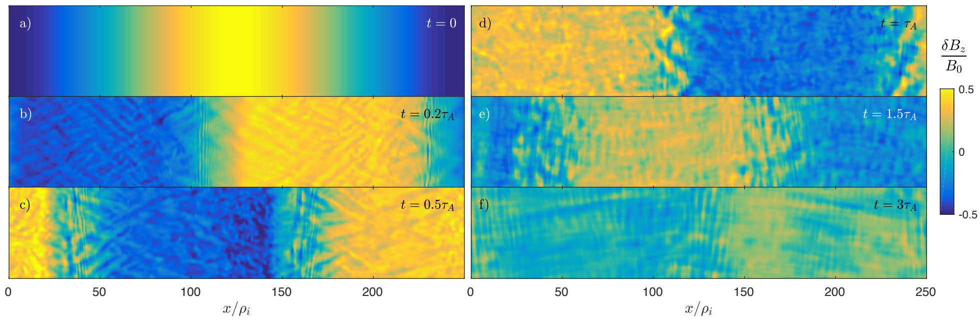

FIGURE 6. Out-of-plane magnetic perturbation $\delta B_z/B_0$ for a rightwards propagating shear-Alfvén traveling wave (initial conditions (2.6)) with $\lambda_A = 250\rho_i$ at a succession of times in its evolution. Note the significant decay of the wave by $t = 3\tau_A$.

(more specifically $\nu_c/\omega_A \sim (\lambda_A/\rho_i)^{\alpha}$ with $\alpha \approx 0.75$ for $\lambda_A/\rho_i \geqslant 250$). If this scaling continued indefinitely, at yet higher λ_A/ρ_i, the wave would reach a point at which the scattering was so strong that the anisotropy returned to $\Delta p \sim 0$ before the large-scale δB_z had dissipated. However, this is also not a viable solution in the $\lambda_A/\rho_i \to \infty$ limit: it requires that the microscale fluctuations, which cause the scattering, survive indefinitely (because the SA wave period $\tau_A = (\lambda_A/\rho_i)\Omega_i^{-1}$ increases with λ_A).

(ii) The scattering at the *latest stages* of the SA wave's decay remains dominated by microscale fluctuations that were excited in the *earliest stages* of SA wave interruption. This is shown by the obvious presence of $k_\parallel\rho_i \sim 1$ modes at the wave nodes in Fig. 1(g), and the high scattering rate in the same regions in Fig. 2(d). Because the characteristic timescale of the SA wave increases with λ_A/ρ_i, while the timescales associated with the oblique firehose modes' evolution do not, the presence of $k_\parallel\rho_i \sim 1$ fluctuations at the nodes suggests the scale separation is not yet asymptotic.†

We thus conclude that either the scaling shown in Fig. 5, or the wave behavior itself, must change at yet higher λ_A/ρ_i. The details of how this occurs depend directly on how oblique firehose modes decay into parallel Alfvénic modes and scatter particles, physics that is currently poorly understood (see §5 for more discussion). This emphasizes how in some situations, the details of the smallest scales in a high-β plasma control the dynamics of the largest scales. What occurs at yet higher λ_A/ρ_i will be the subject of future work, using both simplified simulations of firehose decay and SA-wave simulations.

4. Traveling shear-Alfvén wave

In this section, we discuss the evolution of SA traveling waves. The discussion here is deliberately more concise than that related to the SA standing wave in §3, because it seems likely that the observed behavior is less generically relevant to Alfvénic turbulence (see §2.2.1).

Figure 6 illustrates the spatiotemporal evolution of a (rightwards-moving) traveling wave (initial conditions (2.7)) at $\lambda_A/\rho_i = 250$. As discussed extensively in Squire *et al.* (2017) (see §4 of that paper), traveling-SA-wave dynamics differ from standing-SA-wave dynamics because $\langle dB/dt\rangle = 0$ in a linear traveling SA wave (B is increasing in some regions, and decreasing in others). This implies that a global (spatially constant) pressure anisotropy only develops as the wave decays, meaning it takes longer than the standing

† Unless the are being continuously driven, which does not appear to be the case, because the plasma is apparently stable in these regions; see Fig. 2(c) and §5.

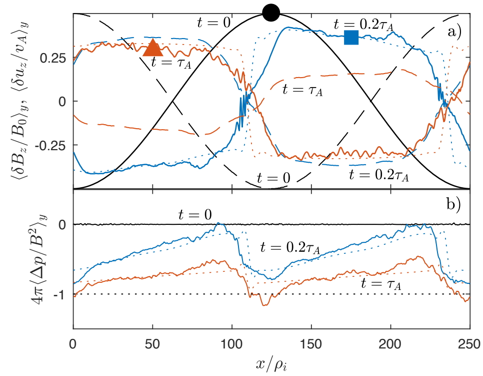

FIGURE 7. Evolution of the traveling wave shown in Fig. 6. In panel (a), we show the y-averaged $\delta B_z/B_0$ (solid lines) and $\delta u_z/v_A$ (dashed lines), at $t/\tau_A = 0$ (black lines; circle marker), $t/\tau_A = 0.2$ (blue lines; square marker), and $t/\tau_A = 1$ (red lines; triangular marker). The markers indicate the same positions on the wave as it propagates to the right. In panel (b), we show the y-averaged firehose parameter $4\pi\Delta p/B^2$ at the same times. The dotted lines in both panels show the evolution in an equivalent 1-D Landau-fluid simulation at $\beta_i = 100$.

wave to reach the firehose limit and only does so in isolated regions of space (where Δp is most negative).

As in §3, it is helpful to divide the wave evolution into five stages:

(i) The spatially dependent dB/dt creates an anisotropy that varies in space as $\Delta p(x) \sim \beta^{1/2}\delta B_z^2 \sin(2k_\parallel x)$, because B changes locally in space as the wave propagates. The heat fluxes play an important role in determining this form of Δp, viz., Δp would be a factor $\sim \beta^{1/2}$ larger (and exciting firehose and mirror instabilities) if not for heat fluxes (Squire *et al.* 2017).

(ii) Due to pressure-anisotropy damping and nonlinear Landau damping (Hollweg 1971; Stoneham 1981; Flå *et al.* 1989), this Δp damps the wave at a rate $\sim \int d\boldsymbol{x}\, \Delta p\, d\ln B/dt$ (Squire *et al.* 2017). This damping causes $\langle B\rangle$ to decrease, and thus also creates a global anisotropy $\langle \Delta p\rangle < 0$.

(iii) Because the Alfvén speed is modified for $\Delta p < 0$, viz.,

$$(v_A)_{\Delta p} = v_A\sqrt{1 + 4\pi\Delta p/B^2}, \tag{4.1}$$

the waves slows down, with its velocity perturbation δu_z decaying faster than its magnetic perturbation δB_z.

(iv) Around the wavefronts, where dB/dt is largest and Δp is most negative, the wave excites oblique firehose modes. These evolve and scatter particles in a similar way to the standing wave.

(v) The particle scattering allows the magnetic perturbation of the (slowly moving) SA wave to decay, with Δp close to the firehose limit.

As for the standing wave, it is the decay of oblique firehose modes into small-scale parallel ($k_\parallel \rho_i \sim 1$) Alfvénic fluctuations (stages (iv) and(v)) that causes the biggest differences between the kinetic simulation and 1-D LF predictions (Squire *et al.* 2017). However, because the firehose fluctuations are excited only in isolated regions of space (around the wavefronts), the scattering is weaker than for the standing wave, and the wave decays correspondingly more slowly.

The stages discussed above can also be seen in Figs. 7 and 8, which show the 1-D (y-averaged) wave profiles at three times from Fig. 6, and the time evolution of the scattering rate and wave parameters, respectively. For example, stages (i)–(iii) are

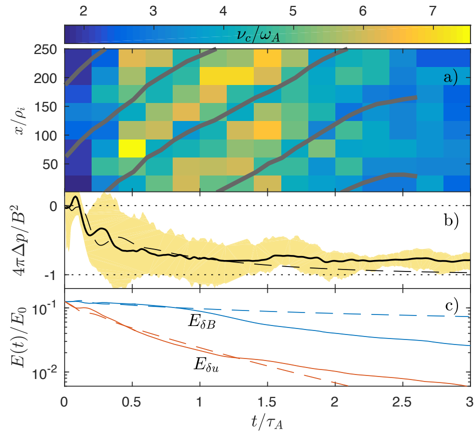

FIGURE 8. (a) Scattering rate ν_c/ω_A of the traveling wave in Fig. 6 as a function of x and t. The grey lines the wave fronts, which is where $\delta B_z \approx 0$ and is close to where Δp is most negative. (b) Time evolution of the spatially averaged firehose parameter $\langle 4\pi\Delta p/B^2\rangle$. The shaded region indicates the range of $4\pi\Delta p/B^2$ seen across the wave profile (i.e., the range seen in Fig. 7(b)), which illustrates when the wave can excite firehose modes. (c) Energy of the magnetic perturbation $E_{\delta B} = \int d\boldsymbol{x}\, \delta B_z^2/8\pi$ (blue) and kinetic energy $E_{\delta u} = \int d\boldsymbol{x}\, \rho\, \delta u_z^2/2$ (red), normalized by $E_0 = \int d\boldsymbol{x}\, B_0^2/8\pi$. In panels (b) and (c), we also plot the results from the equivalent 1-D Landau-fluid simulation (dashed lines; see also Fig. 7), for comparison.

evident in the δu_z and Δp profiles Fig. 7 at $t/\tau_A = 0.2$, and also through the globally averaged parameters shown in Fig. 8(b) and (c). Similarly, the position of the wavefronts (Fig. 8(a)) illustrates how the wave slows down. Throughout these earlier stages of SA wave evolution, the dynamics are described well by the predictions of an equivalent 1-D LF model,† even though finite Larmor radius effects (which were not included in the LF model) are significant at this scale separation. This comparison is shown in Fig. 7 (dotted lines) and Fig. 8(b) and (c) (dashed lines). The good agreement with LF predictions for $t/\tau_A \lesssim 1$ implies that the analytic estimates for the wave evolution and decay rates derived in Squire *et al.* 2016 §4.2 should apply to the earlier stages of large-scale SA wave evolution.

As shown in Fig. 8(b), by $t/\tau_A \approx 0.3$, Δp has reached the parallel firehose limit in regions of space around the wavefronts (see, e.g., Fig. 7(b) at $t/\tau_A = 1$ at $x/\rho_i \approx 120$, or the clear appearance of oblique firehose modes at the same location in Fig. 6(d)). The preferential excitation of firehose modes around the wavefront regions simply results from the large dB/dt in these regions (note also the angular shape of δB_z in Fig. 7(a), which minimizes dB/dt over much of the wave). Following the excitation of firehose modes, Fig. 8(a) shows that the particle scattering is strongest *behind* the wavefronts. We interpret this as being due to the time delay required for oblique firehose modes to transition into smaller-scale $k_\| \rho_i \sim 1$ Alfvénic fluctuations that scatter particles, as occurred for the standing wave (see also §5.2 and Fig. 10). These long-lived parallel modes are visible in Fig. 6 at later times, and small-scale (although more disordered) fluctuations are also visible at earlier times between the wavefronts (e.g., Fig. 6(c) and (d)). Note that the overall scattering rate caused by the traveling wave, $\nu_c/\omega_A \approx 4$ is

† The reader may notice that here we compare to a collisionless LF model, whereas for the standing wave we compared to a collisional Braginskii one. This is simply because for the traveling wave, we compare the early stages of evolution (which are nearly collisionless) with the LF model, while for the standing wave, we compared the later stages of decay (which were moderately collisional due to microscale scattering) with the Braginskii model.

significantly lower than for a standing wave at $\lambda_A/\rho_i = 250$ ($\nu_c/\omega_A \approx 10$, see Fig. 5), and the traveling wave's δB_z decays correspondingly more slowly. This is likely because the firehose modes are excited only briefly in isolated regions of space around the wavefronts, rather than across the whole wave at once. The particle scattering allows the large-scale $\delta B_\perp$ to decay (maintaining $\langle \Delta p \rangle < 0$ requires $\langle dB/dt \rangle < 0$ if $\nu_c \neq 0$; see Fig. 8(b) and (c) for $t/\tau_A \gtrsim 1$), and the wave's final stages of decay (e.g., Fig. 6(f)) are similar to the standing wave.

5. The decay of oblique firehose fluctuations and emergence parallel Alfvénic fluctuations

As stressed throughout the preceding sections, the evolution of oblique firehose modes as the plasma becomes firehose stable is of utmost importance for the subsequent evolution of the large-scale SA wave. In particular, we have seen a ubiquitous occurrence of small-scale parallel fluctuations ($k_\perp \sim 0$, $k_\| \rho_i \sim 1$), which apparently emerge through the decay oblique firehose modes as the anisotropy evolves above $\Delta p > -B^2/4\pi$. We are left with several questions, the answers to which have a key bearing on the behavior of SA waves in the $\lambda_A/\rho_i \to \infty$ limit (see §3.2): What causes the emergence of these fluctuations (as opposed to the behavior seen in driven simulations, e.g., Kunz *et al.* 2014*a*)? For how long do they persist and scatter particles? How does their behavior depend on bulk plasma parameters (e.g., Δp, heat fluxes)? Here, we illustrate two key points about their evolution, leaving more detailed investigation to future work. These are: (i) (§5.1) that they are Alfvénic in character, and persist over long time periods because they are nonlinearly stabilized against cyclotron damping; and (ii) (§5.2) that the modes occur as a result of the quasi-linear saturation of oblique firehose modes when the anisotropy is free to evolve (i.e., Δp is not forced by a large-scale dB/dt from shear or compression).

5.1. *Linear properties and nonlinear stabilization against cyclotron damping*

An obvious starting point, given the relatively coherent appearance of the the parallel fluctuations in the SA-wave simulations (e.g., Fig. 1(d)–(g)), is to examine the linear physics of modes with $k_\| \rho_i \sim 1$, $k_\perp \sim 0$ at $\beta_i \gg 1$. Some other relevant properties to help with their identification include: (i) they are almost completely static in space and time (i.e., their real frequency ω is almost zero); (ii) there is very little associated velocity perturbation (this is suggested by (i)); and (iii) they are perpendicular ($\delta\tilde{\boldsymbol{B}} \sim \delta\tilde{\boldsymbol{B}}_\perp$), and likely circularly polarized† $\delta\tilde{B}_z \sim \delta\tilde{B}_y$.

The dispersion relation of Alfvén and whistler branches (i.e., the continuation of the shear-Alfvén wave to small scales) at $k_\perp = 0$ and $\beta_i = 100$, is shown in Fig. 9(a). We use the HYDROS dispersion solver (Told *et al.* 2016*a*,*b*), which solves the hybrid-kinetic dispersion relation and so excludes electron kinetic physics‡ (as is also the case in our PIC simulations). We see that the Alfvén branch modes (solid and dashed lines)—which are very low frequency ($\omega \sim 0.01\Omega_i$), perpendicular, and circularly polarized (not shown)—appear similar to the observed fluctuations, aside from their very high damping rate for

† The handedness of their polarization is hard to make out: because of property (i) they do not have an obvious direction of propagation.

‡ Comparison with a fully kinetic dispersion relation (Klein, private communication; Klein & Howes 2015), has shown that the electron contribution is negligible at these parameters, as also expected based on previous works (Quataert 1998; Quataert & Gruzinov 1999; Told *et al.* 2016*b*).

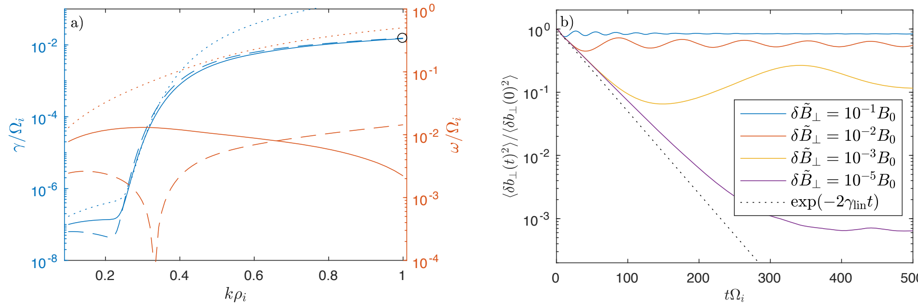

FIGURE 9. Linear and nonlinear properties of $k_\| \rho_i \approx 1$, $k_\perp = 0$ fluctuations in a $\beta_i = 100$ plasmas. (a) shows the linear dispersion relation (calculated using the HYDROS solver; Told *et al.* 2016*a*) as a function of $k_\|\rho_i$. The left-hand axis (blue curves) shows the mode damping rate γ/Ω_i, while the right-hand axis (red curves) shows the real part of the wave frequency ω/Ω_i. We show three sets of dispersion relations: the Alfvénic branch at $\Delta p = 0$ (solid lines), the Alfvénic branch at $4\pi\Delta p/B^2 = -0.8$ (dashed lines), and the whistler branch at $\Delta p = 0$ (dotted lines). Note the very low frequencies of the Alfvénic branch modes (due to the high β), the near independence of the damping rates on Δp, and the strong damping of whistler modes. (b) shows the evolution of nonlinear $k_\|\rho_i = 1$ fluctuations at a variety of initial amplitudes (see text for full description). Each curve shows the magnetic perturbation energy, normalized by its initial value, as a function of time. The dotted curve indicates the expected decay rate, taken from the linear result $\gamma_{\rm lin}$ in panel (a) (the black circle at $k_\|\rho_i = 1$). While at very low amplitude, the PIC simulation results agrees with the linear prediction, there is a clear nonlinear stabilization against decay. For fluctuation amplitudes seen in Figs. 1 and 6 ($\delta\tilde{B}_\perp \sim 0.1B_0$), this would effectively render any linear damping of $k_\|\rho_i \sim 1$ fluctuations unnoticeable.

$k_\|\rho_i \gtrsim 0.3$ due to cyclotron damping.¶ They are also mostly independent of the imposed Δp (c.f., solid and dashed lines in Fig. 9(a)). The whistler branch mode (dotted lines) is also perpendicular and circularly polarized, but its high frequency, $\omega/\Omega_i \approx 0.3$, suggests that this mode is not related to the parallel fluctuations seen in the simulations (it is also strongly damped for $k_\|\rho_i \gtrsim 0.3$). These properties generally match trends seen at lower β in previous works (Gary 2004; Told *et al.* 2016*a*).

With these indications that the observed parallel fluctuations are indeed Alfvénic, how do they survive in the SA wave simulations, given their strong linear damping ($\gamma \sim 0.01\Omega_i$)? The answer appears to lie in a nonlinear saturation of the cyclotron damping mechanism, which stabilizes the mode decay at even very small amplitudes (a similar effect also occurs to a lesser degree at low β; Gary & Saito 2003). A simple numerical experiment to test this is shown in Fig. 9(b). In a square domain, of size $L_x = L_y = 50\rho_i$, we initialize $\delta\tilde{B}_\perp$ fluctuations (in B_y and B_z, $\pi/2$ out of phase), at $k_\|\rho_i = 1$, $k_\perp = 0$, with a variety of initial amplitudes from $\delta\tilde{B}_\perp(0) = 10^{-5}B_0$ to $\delta\tilde{B}_\perp(0) = 10^{-1}B_0$. The results, shown in Fig. 9(b), indicate that although very low amplitude fluctuations decay linearly as expected (c.f., black dotted line), at higher amplitudes the decay is quickly nonlinearly stabilized. The effect is sufficiently strong that for the small-scale fluctuation amplitudes seen in the SA wave simulations ($\delta\tilde{B}_\perp \sim 0.1B_0$; see Fig. 1), the linear phase of decay would effectively be unobservable. This explains the presence of these modes in

¶ A convincing argument for the importance of the cyclotron resonance in the damping comes from simple analytic estimates. In particular, Eq. (11-8) in Stix (1992), gives the cyclotron damping rate for parallel modes, $\gamma/\omega \approx 0.9\,(\omega/\Omega_i)\,\beta^2(k_\|\rho_i)^{-5}e^{-1/(k_\|\rho_i)}$, where we assumed $\omega \ll \Omega_i$ and $\gamma \ll \omega$. Comparison of this expression with Fig. 9(a) shows that the two agree when $\gamma \ll \omega$.

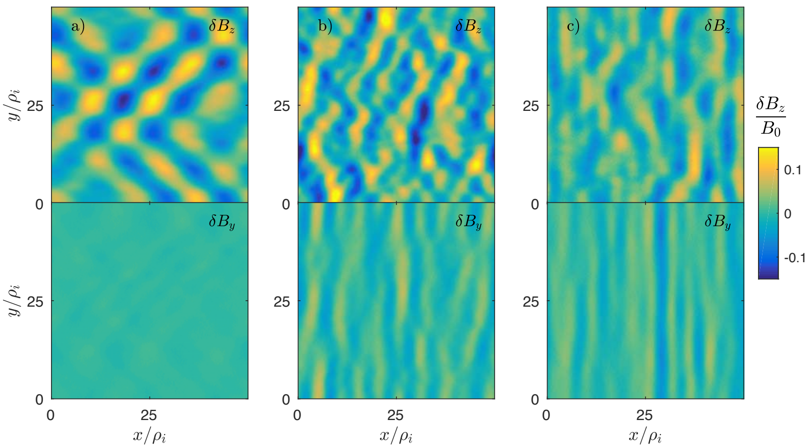

FIGURE 10. Magnetic perturbation $\delta\tilde{B}_z$ (top panels) and $\delta\tilde{B}_y$ (bottom panels) pictured at various times in the numerical experiment described in §5.2 (firehose evolution in a homogenous domain, with an initial anisotropy $4\pi\Delta p/B^2 = -1.3$ that is free to evolve). Panel (a) shows the perturbations at $t = 800\Omega_i^{-1}$, which is just after the firehose modes have pushed Δp above the parallel firehose limit. Panels (b) and (c) show the field at $t = 2000\Omega_i^{-1}$ and $t = 3000\Omega_i^{-1}$, illustrating the tendency for the oblique modes to move to smaller scale and become parallel.

Figs. 1 and 6, despite the fact that linear Alfvénic fluctuations are strongly damped at these parameters.

In the context of large-scale SA waves, we are left with some interesting questions. For example, as $\lambda_A/\rho_i \to \infty$, does the amplitude of the parallel modes ever become small enough such that they are linearly damped before being stabilized, and they no longer scatter particles? Unfortunately, a more detailed understanding of the nonlinear stabilization mechanism (and the initial oblique firehose excitation; see below) is required to answer this, and we leave further investigation to future work.

5.2. *Appearance from oblique firehose decay*

In the SA-wave simulations, Figs. 1–6, there are a variety of complicating factors. For example, the background large-scale plasma parameters ($\boldsymbol{B}$ and Δp) are inhomogenous and this creates heat fluxes along the magnetic field. Because such effects could enable new instabilities (e.g., the gyrothermal instability; Schekochihin *et al.* 2010), or influence the evolution of the small-scale firehose modes, it is important understand whether the observed behavior arises only in specific situations (i.e., in nonlinear SA waves), or whether it is more generic.

In this section, we explore these issues using a simple numerical experiment. We find that the prevalence of $k_\parallel\rho_i \sim 1$ fluctuations occurs as a result of the decay of oblique firehose fluctuations (at amplitudes before they saturate nonlinearly; see Melville *et al.* 2016) in a system where the anisotropy is free to evolve, viz., heat fluxes and/or inhomogeneity do not play a major role. The setup is as follows. In a homogenous domain, of size $L_x = L_y = 50\rho_i$, we initialize with low-amplitude oblique magnetic perturbations $\delta\tilde{B}_z$ with $k\rho_i \approx 0.5$, $k_\perp = k_\parallel$. We also initialize with a homogenous anisotropy $4\pi\Delta p/B^2 = -1.3$ that is firehose unstable. We use a resolution ~ 4 times that used in the SA wave simulations, $\Delta x \approx 0.083\rho_i$, to ensure that the scale of the small-scale modes is not being affected by the grid scale, and use 256 particles per cell (we have also run at the standard resolution and $N_{\rm ppc} = 4096$ and see similar behavior).

The results are illustrated in Fig. 10 at several times. The growth of the oblique firehose instability first pushes the bulk anisotropy above the firehose limit (to $4\pi\Delta p/B^2 \approx -0.9$) at $t = 800\Omega_i^{-1}$ (Fig. 10(a)). The residual firehose fluctuations then evolve to become smaller scale in the (now stable) plasma, becoming more elongated in the parallel direction as they do so (Fig. 10(b)). Fluctuations in $\delta\tilde{B}_y$ are particularly coherent in parallel direction, and of about half the amplitude of the $\delta\tilde{B}_z$ fluctuations,† which is also seen in the SA wave simulations (not shown). These $k_\parallel\rho_i \sim 1$ fluctuations continue to become more coherent and evolve quite slowly in time, as shown in Fig. 10(c).

Overall, this behavior, and the morphology of the fluctuations, is similar that seen in the SA simulations (Figs. 1 and 6). This leads us to conclude that the decay of oblique firehose modes into long-lived $k_\perp \sim 0$, $k_\parallel\rho_i \sim 1$ Alfvénic fluctuations is a generic consequence of their evolution in a freely evolving anisotropy—i.e., an anisotropy that is not driven by a large-scale dB/dt—as occurs in the regions around the nodes of the SA standing wave (see Fig. 1(c)-(f)). This evolution differs somewhat from that of firehose fluctuations that have been driven to saturation in a constant shear flow (Kunz *et al.* 2014*a*; Melville *et al.* 2016),‡ but further investigation and simplified numerical experiments are needed to better address these issues.

6. Discussion and conclusions

We have presented hybrid-kinetic simulations of large-amplitude, long-wavelength Alfvénic perturbations in a collisionless plasma. This study is motivated by gaining a better understanding of Alfvénic turbulence in high-β low-collisionality plasmas, conditions that are expected to be common across diverse astrophysical environments (Rosin *et al.* 2011; Bruno & Carbone 2013; Yuan & Narayan 2014). The single, isolated shear-Alfvén wave is perhaps the simplest laboratory possible in which to study the self-consistent interaction between large-scale, MHD dynamics, and the microscale fluctuations that erupt due to kinetic instabilities. Because of this simplicity, such studies can act as a bridge between homogenous simulations of high-β microinstabilities (e.g., Matteini *et al.* 2006; Kunz *et al.* 2014*a*; Riquelme *et al.* 2015; Sironi & Narayan 2015), which are in some cases too idealized to see certain important effects, and kinetic turbulence simulations (e.g., Rincon *et al.* 2016; Franci *et al.* 2015; Kunz *et al.* 2016), which suffer from reduced scale separations and the difficulty of diagnosing their extremely complex dynamics.

Using a realistic method that includes fully kinetic ions, our simulations have demonstrated four interesting aspects of collisionless high-β dynamics:

- That linearly polarized shear-Alfvénic perturbations do not exist in their linear wave form in a collisionless plasma, above the amplitude limit $\delta B_\perp/B_0 \sim \beta^{-1/2}$ (Squire *et al.* 2016).
- That the details of microinstability saturation has a crucial influence on the largest-scales $\lambda \gg \rho_i$. In particular, we have seen that MHD-scale shear-Alfvén waves (e.g., $\lambda_A = 1000\rho_i$) depend strongly on how oblique firehose fluctuations evolve as the plasma moves into the stable regime $\Delta p \gtrsim -B^2/4\pi$.
- That dynamics can be significantly nonlocal, viz., that microscale fluctuations or plasma parameters in one region of space may affect the dynamics in a nearby region. This is because the thermal speed is large compared to the Alfvén speed in high-β plasmas ($v_{\mathrm{th},i} \sim \beta^{1/2} v_A$).

† This difference between in-plane and out-of-plane $\delta\tilde{B}_\perp$ fluctuations suggests that the detailed evolution may be affected by our choice of 2-D geometry, and 3-D simulations will be needed to address questions about the morphology of the fluctuations with more confidence.

‡ For example, compare the spectrum in Fig. 3 at $t/\tau_A = 0.6$, which peaks at $k\rho_i \approx 1$, with the magnetic spectrum of saturated firehose turbulence shown in Fig. 8(a) of Kunz *et al.* (2014*a*).

• That energy in large-scale perpendicular perturbations can be directly converted into thermal energy and microscale fluctuations, without the usual route through a turbulent cascade.

These points have been illustrated by studying both standing SA waves and traveling SA waves. We see that standing-wave dynamics (§3) evolve to resemble SA waves in the Braginskii regime (Squire *et al.* 2017), because of the strong particle scattering that occurs as oblique firehose modes evolve into smaller scale, parallel fluctuations ($k_{\|}\rho_i \sim 1$, $k_{\perp} \sim 0$). Interestingly, this scattering is strongest at the wave nodes, where the plasma is most stable, but is able to cause the global decay of the large-scale SA wave due to the nonlocality of high-β dynamics. Traveling-wave dynamics (§4) are nearly collisionless initially, and are well described by the predictions of a simple 1-D Landau-fluid model (Snyder *et al.* 1997; Squire *et al.* 2017); however, once the wave builds up a global negative anisotropy, it also excites oblique firehose modes that transition into small-scale parallel fluctuations, and the final stages of wave decay resemble the standing wave. The appearance of small-scale parallel fluctuations in both cases prompted us to examine these in more detail in §5, where we found that the nonlinear stabilization against cyclotron damping plays a key role in their longevity, and that they evolve naturally from oblique firehose modes when the pressure anisotropy is not driven by a shear flow or compression.

Unfortunately, as discussed in detail in §3.2, our simulations cannot fully address what occurs at yet higher λ_A/ρ_i. This will depend on how oblique firehose modes decay into parallel Alfvénic modes and scatter particles. This process is currently poorly understood despite hints in §5 that this physics is a generic feature of oblique firehose decay. Nonetheless, it is clear that SA wave interruption provides a robust mechanism for the dissipation of energy directly from large-scale perturbations into heat and microinstabilities. This strong deviation from the predictions of MHD models could significantly impact the turbulent dynamics of high-β weakly collisional plasmas, in a way reminiscent of the scenario suggested in Kunz *et al.* (2010): large-amplitude perturbations (on scales less than the mean free path) experience a sudden damping into heat and microscale fluctuations, while small-amplitude perturbations happily undergo a standard Alfvénic cascade. One concrete way to probe such physics in simplified simulations might be a Landau-fluid model with pressure-anisotropy limiters (Sharma *et al.* 2006) that enhance the collisionality to a rate that is determined by the large-scale Alfvén frequency. However, further speculation on such models is beyond the scope of this work, and may require a better understanding of the $\lambda_A/\rho_i \to \infty$ limit and/or the fate of Alfvénic velocity perturbations, if one hopes make confident progress in this endeavor.

It is a pleasure to thank S. Balbus, S. Bale, C. H. K Chen, S. Cowley, B. Dorland, G. Hammett, K. Klein, F. Rincon, L. Sironi, and M. Strumik for useful and enlightening discussions. JS, AAS, and MWK would like to thank the Wolfgang Pauli Institute in Vienna for its hospitality on several occasions. JS was funded in part by the Gordon and Betty Moore Foundation through Grant GBMF5076 to Lars Bildsten, Eliot Quataert and E. Sterl Phinney. EQ was supported by Simons Investigator awards from the Simons Foundation and NSF grant AST 13-33612. AAS was supported in part by grants from UK STFC and EPSRC. MWK was supported in part by NASA grant NNX16AK09G and US DOE Contract DE-AC02-09-CH11466.

Appendix A. Numerical tests

In this appendix, we outline various numerical tests that we used to ensure the accuracy of the nonlinear SA wave simulations in the main text. We start by discussing a series of

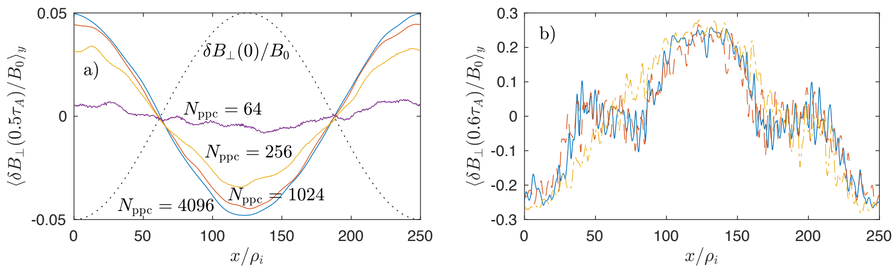

FIGURE 11. (a) Numerical scaling with particles per cell, for linear standing waves (initial conditions (2.6), with $\delta b = 0.05$) in *Pegasus* at $\lambda_A/\rho_i = 250$. The lines show the y-averaged $\delta B_z/B_0$ at $t/\tau_A = 0.5$ ($t = 1250\Omega_i^{-1}$) for simulations with the numerical parameters given in §2.2, using $N_{\rm ppc} = 4096$ (blue line), $N_{\rm ppc} = 1024$ (red line), $N_{\rm ppc} = 256$ (yellow line), or $N_{\rm ppc} = 64$ (purple line). The dotted black line shows the initial conditions (2.6). (b) Numerical scaling with particles per cell for nonlinear standing waves. The setup is identical to the standing-wave simulation discussed in §3, except that we use $\lambda_A/\rho_i = 250$. We show the y-averaged magnetic perturbation $\delta B_z/B_0$ at $t/\tau_A = 0.6$, for $N_{\rm ppc} = 4096$ (blue solid line), $N_{\rm ppc} = 1024$ (red dashed line), $N_{\rm ppc} = 256$ (yellow dot-dashed line).

tests to ensure the correct propagation of linear SA waves in *Pegasus*, then consider the scaling of nonlinear ($\delta b = 0.5$) SA waves with the number of particles per cell, $N_{\rm ppc}$. We finish with brief discussion of the unphysical grid heating seen in Fig. 4.

A.1. *Linear SA wave tests*

In order to be confident in nonlinear results, it is important to ensure that linear long-wavelength SA waves are accurately propagated by *Pegasus*. We have run a variety of such linear tests, for both standing waves (from an initial magnetic perturbation, (2.6), or an initial velocity perturbation) and for traveling waves (initial conditions 2.7). We use the same numerical parameters as discussed in §2.2, but vary λ_A/ρ_i (between $\lambda_A/\rho_i = 50$ and $\lambda_A/\rho_i = 1000$) and $N_{\rm ppc}$ (between $N_{\rm ppc} = 16$ and $N_{\rm ppc} = 4096$).†

These tests have shown that large numbers of particles per cell are required for long-wavelength SA waves, due to the build up of noise over the long simulation times required. In particular, we see an unphysical damping of linear SA waves at low ppc, with the $N_{\rm ppc}$ required to accurately propagate a wave at a given λ_A/ρ_i increasing linearly with λ_A/ρ_i. For example, a wave with $\lambda_A/\rho_i = 250$ and $N_{\rm ppc} = 256$ will develop similar errors to a wave with $\lambda_A/\rho_i = 1000$ and $N_{\rm ppc} = 1024$, by a given t/τ_A (but recall, $\tau_A\Omega_i$ increases with λ_A/ρ_i). In Fig. 11(a), we show the effect of this unphysical damping on linear SA standing waves, through the scaling with $N_{\rm ppc}$ at $\lambda_A/\rho_i = 250$. Clearly, at $N_{\rm ppc} = 64$, the simulation is grossly incorrect by $t/\tau_A = 0.5$, while $N_{\rm ppc} = 256$ is marginal and with $N_{\rm ppc} \gtrsim 1024$, linear SA waves are propagated relatively accurately. The scaling seen for traveling waves is very similar. As of yet, it is unclear exactly what causes this unphysical damping, and work is ongoing to better understand its properties.‡

† Note that for smaller scale separations $\lambda_A/\rho_i \lesssim 200$, the differing phase speeds of the Alfvénic and whistler branches of the dispersion relation (see Fig. 9(a)) cause linearly polarized SA waves to differ somewhat from MHD predications, with a δB_y perturbation being created from the initial δB_z perturbation.

‡ Two points are worth mentioning: first, that the unphysical damping is more severe in 1-D domains, and second, that it only occurs when using the δf-PIC method. These properties suggest the damping may be related to a spurious instability that occurs in the δf method. Such instabilities have been found before in different contexts (Wilkie & Dorland 2016; Sturdevant & Parker 2016). However, given the high-β, which implies that very small ($\ll \beta^{-1}$) perturbations

A.2. *Nonlinear SA wave tests*

We have also checked the convergence of nonlinear-SA-wave dynamics with $N_{\rm ppc}$ at $\lambda_A/\rho_i = 250$. In Fig. 11(b), we show the y-averaged $\delta B_z/B_0$ at $t/\tau_A = 0.6$, for a series of standing-wave simulations.¶ The results broadly match what would be expected from linear SA wave calculations (Fig. 11(a)): the solution is effectively converged (there are no discernible difference in the large-scale wave evolution) for $N_{\rm ppc} \gtrsim 1024$, but clear differences are visible at $N_{\rm ppc} \gtrsim 256$.

The number of particles per cell for our fiducial simulations presented in §3 and §4 were chosen based on the linear and nonlinear scalings discussed in the previous paragraph and in §A.1. Given that we have also seen qualitatively similar large-scale dynamics for SA waves with $\lambda_A/\rho_i \in [125, 1000]$ (for example, compare Figs. 2(c) and 11(b)), we are relatively confident that the observed dynamics do not arise due to numerical artifacts. It is also worth reiterating that the small-scale parallel magnetic fluctuations, which played an important role in particle scattering, occur independently of the grid resolution (see Fig. 10) or the alignment of the magnetic field with the grid (not shown).

A.3. *Grid heating and density increase*

A well-known effect in PIC codes is a spurious heating that occurs due to finite-particle noise (Birdsall & Langdon 1991). In the δf method, there is also a corresponding increase in the global density $\langle n_i \rangle$. Here, we simply note that for the fiducial simulations presented in the main text, the relative increase in $\langle n_i \rangle$ is $\sim 0.05\%$ for the $\lambda_A/\rho_i = 1000$ standing-wave simulation in §3, and $\sim 0.1\%$ for the $\lambda_A/\rho_i = 1000$ traveling-wave simulation in §4. We have removed this contribution from $\partial_t E_{\rm th}$ in Fig. 4(a) (by computing $\int d\boldsymbol{x}\, n_i \sum_r \partial_t(\mathit{\Pi}_{rr}/n_i)/2$ as opposed to $\int d\boldsymbol{x} \sum_r \partial_t \mathit{\Pi}_{rr}/2$) but note that its contribution to $\partial_t E_{\rm th}$ is similar in magnitude to the spurious heating shown in Fig. 4(a) (i.e., the difference between the heating and $\partial_t E_{\rm th}$). The nonlinear standing wave tests at $\lambda_A/\rho_i = 250$ (Fig. 11(b)) have shown that the relative grid heating and density increase decrease with $N_{\rm ppc}$ and increase with λ_A/ρ_i (due to the longer simulation times), as expected.

Appendix B. Measurement of the particle scattering

In this appendix, we outline the method used to measure particle scattering in Figs. 2, 5, and 8. The method is based on that of Kunz *et al.* (2014*a*); Melville *et al.* (2016), with some modifications to allow the measurement of the "local" ν_c as a function of space and time.

The method works by calculating the time τ_κ, that it takes μ to change by a factor κ (i.e., $\mu \to \mu\kappa$ or $\mu \to \mu/\kappa$), for a sample of particle tracks saved from the simulation. For those events that occur within a chosen bin in x and t (i.e., $x_{\rm event} \in [x, x + \mathit{\Delta} x]$, $t_{\rm event} \in [t, t + \mathit{\Delta} t]$, where $x_{\rm event}$ and $t_{\rm event}$ denote the spatiotemporal location at which μ changed by a factor of κ from its previous event), we calculate the mean of τ_κ across all particles, which is the maximum likelihood estimate for the exponential distribution e^{-t/τ_κ}.

Evidently τ_κ, the average time required for μ to change by a factor of κ, is related to ν_c^{-1}, but also depends on κ. Defining an unambiguous measure of ν_c is tricky, but based

to f_i must be accurately resolved, the use of the full-f method is not feasible for propagating SA waves for the values of β and scale separations of interest here.

¶ Note that the wave decay is slower compared to at $\lambda_A/\rho_i = 1000$, as discussed in §3.2 (c.f., Fig. 2(d)).

on the evolution of the pressure anisotropy in a collisional plasma $\partial_t \Delta p \sim -\nu_c \Delta p$, it is reasonable to define ν_c^{-1} as $\tau_{\exp(1)}$. However, using $\kappa = \exp(1)$ brings problems: with such a large change in μ there are few events, and one is no longer measuring a local scattering rate because particles can stream between several bins before each event. We thus rescale τ_κ according to

$$\nu_c^{-1} = \tau_{\exp(1)} = \left(\frac{1}{\ln \kappa}\right)^2 \tau_\kappa, \tag{B 1}$$

an estimate that arises from assuming that $\ln \mu$ undergoes a random walk.† For measurements in the text, we choose $\kappa = 1.2$ because it is small enough that there are many "events" (factor κ changes in μ) per bin, but large enough that any recorded change in μ is indeed due to scattering from microscale fluctuations. For all bins in Fig. 2, and all but the lowest collisionality bins (for $t/\tau_A < 0.2$, or $t/\tau_A \gtrsim 2.5$) in Fig. 8(a), we have checked that there are at least 2 events per particle per bin, which ensures that it is indeed a local value of ν_c that is being measured using this method. The results in Figs. 2, 5, and 8(a) are broadly unchanged for any κ in the range $1.1 \lesssim \kappa \lesssim 2$.

REFERENCES

Alfvén, H 1942 Existence of electromagnetic-hydrodynamic waves. *Nature* **150** (3), 405–406.

Bale, S D, Kasper, J C, Howes, G G, Quataert, E, Salem, C & Sundkvist, D 2009 Magnetic fluctuation power near proton temperature anisotropy instability thresholds in the solar wind. *Phys. Rev. Lett.* **103** (2), 211101.

Birdsall, C. K. & Langdon, A. B. 1991 *Plasma Physics via Computer Simulation*. Adam Hilger, Bristol, England.

Boldyrev, S 2006 Spectrum of magnetohydrodynamic turbulence. *Phys. Rev. Lett.* **96**, 11502.

Boris, J. P. 1970 Relativistic plasma simulation: optimization of a hybrid code. In *Proc. Fourth Conf. Num. Sim. Plasmas*, pp. 3–67. Naval Res. Lab.

Braginskii, S I 1965 Transport processes in a plasma. *Rev. Plasma Phys.* **1**, 205–.

Bruno, Roberto & Carbone, Vincenzo 2013 The solar wind as a turbulence laboratory. *Living Rev. Solar Phys.* **10**.

Chandrasekhar, S., Kaufman, A. N. & Watson, K. M. 1958 The stability of the pinch. *Proc. R. Soc. London A* **245**, 435–455.

Chen, C. H. K. 2016 Recent progress in astrophysical plasma turbulence from solar wind observations. *J. Plasma Phys.* **82** (6), 535820602.

Chen, C. H. K., Matteini, L., Schekochihin, A. A., Stevens, M. L., Salem, C. S., Maruca, B. A., Kunz, M. W. & Bale, S. D. 2016 Multi-species measurements of the firehose and mirror instability thresholds in the solar wind. *Astrophys. J. Lett.* **825**, L26.

Chen, Y & Parker, SE 2003 A delta f particle method for gyrokinetic simulations with kinetic electrons and electromagnetic perturbations. *J. Comp. Phys.* **189** (2), 463–475.

Cheng, J., Parker, S. E., Chen, Y. & Uzdensky, D. A. 2013 A second-order semi-implicit δf method for hybrid simulation. *J. Comp. Phys.* **245**, 364–375.

Cramer, Neil F 2011 *The Physics of Alfvén Waves*. John Wiley & Sons.

Evans, C. R. & Hawley, J. F. 1988 Simulation of magnetohydrodynamic flows - A constrained transport method. *Astrophys. J.* **332**, 659–677.

Flå, T., Mjølhus, E. & Wyller, J. 1989 Nonlinear Landau damping of weakly dispersive circularly polarized MHD waves. *Phys. Scripta* **40** (2), 219.

Foote, E A & Kulsrud, R M 1979 Hydromagnetic waves in high beta plasmas. *Astrophys. J.* **233**, 302–316.

Franci, L., Landi, S., Matteini, L., Verdini, A. & Hellinger, P. 2015 High-resolution

† An examination of the statistics of $\ln \mu$ shows that it does not, in fact, undergo a true random walk, which is perhaps not surprising. Thus, the scaling (B 1) is not completely correct, but it captures the general trends and so is reasonable for our purposes here.

hybrid simulations of kinetic plasma turbulence at proton scales. *Astrophys. J.* **812**, 21, arXiv: 1506.05999.

Gary, S Peter 2004 Alfvén-cyclotron fluctuations: Linear Vlasov theory. *J. Geophys. Res* **109** (A6), 1483–10.

Gary, S Peter & Saito, Shinji 2003 Particle-in-cell simulations of Alfvén-cyclotron wave scattering: Proton velocity distributions. *J. Geophys. Res* **108** (A5), 373–10.

Gekelman, W., Vincena, S., Compernolle, B. Van, Morales, G. J., Maggs, J. E., Pribyl, P. & Carter, T. A. 2011 The many faces of shear Alfvén waves. *Physics of Plasmas* **18** (5), 055501.

Goldreich, P & Sridhar, S 1995 Toward a theory of interstellar turbulence. 2: Strong alfvenic turbulence. *Astrophys. J.* **438**, 763–775.

Hellinger, P & Matsumoto, H 2000 New kinetic instability: Oblique Alfvén firehose. *J. Geophys. Res* **105** (A), 10519–10526.

Hellinger, Petr & Trávníček, Pavel M 2008 Oblique proton fire hose instability in the expanding solar wind: Hybrid simulations. *J. Geophys. Res* **113**, A10109.

Hollweg, Joseph V 1971 Nonlinear Landau damping of Alfvén waves. *Phys. Rev. Lett.* **27** (2), 1349–1352.

Klein, K G & Howes, G G 2015 Predicted impacts of proton temperature anisotropy on solar wind turbulence. *Phys. Plasmas* **22** (3), 032903.

Kunz, M W, Schekochihin, A A, Cowley, S C, Binney, J J & Sanders, J S 2010 A thermally stable heating mechanism for the intracluster medium: turbulence, magnetic fields and plasma instabilities. *Mon. Not. R. Astron. Soc.* **410** (4), 2446–2457.

Kunz, Matthew W, Schekochihin, Alexander A & Stone, James M 2014*a* Firehose and mirror instabilities in a collisionless shearing plasma. *Phys. Rev. Lett.* **112** (2), 205003.

Kunz, Matthew W, Stone, James M & Bai, Xue-Ning 2014*b* Pegasus: A new hybrid-kinetic particle-in-cell code for astrophysical plasma dynamics. *J. Comp. Phys.* **259**, 154–174.

Kunz, Matthew W, Stone, James M & Quataert, Eliot 2016 Magnetorotational turbulence and dynamo in a collisionless plasma. *Phys. Rev. Lett.* **117** (2), 235101.

Mallet, A. & Schekochihin, A. A. 2017 A statistical model of three-dimensional anisotropy and intermittency in strong Alfvénic turbulence. *Mon. Not. R. Astron. Soc.* **466**, 3918–3927.

Matteini, L., Landi, S., Hellinger, P. & Velli, M. 2006 Parallel proton fire hose instability in the expanding solar wind: Hybrid simulations. *J. Geophys. Res.: Space Phys.* **111**, A10101.

Melville, Scott, Schekochihin, Alexander A & Kunz, Matthew W 2016 Pressure-anisotropy-driven microturbulence and magnetic-field evolution in shearing, collisionless plasma. *Mon. Not. R. Astron. Soc.* **459** (3), 2701–2720.

Ogilvie, Gordon I. 2016 Astrophysical fluid dynamics. *J. Plasma Phys.* **82** (3), 205820301.

Parker, E. N. 1958 Dynamical instability in an anisotropic ionized gas of low density. *Phys. Rev.* **109**, 1874–1876.

Quataert, Eliot 1998 Particle heating by Alfvénic turbulence in hot accretion flows. *Astrophys. J.* **500** (2), 978–991.

Quataert, Eliot & Gruzinov, Andrei 1999 Turbulence and particle heating in advection-dominated accretion flows. *Astrophys. J.* **520** (1), 248–255.

Quest, K. B. & Shapiro, V. D. 1996 Evolution of the fire-hose instability: Linear theory and wave-wave coupling. *J. Geophys. Res* **101**, 24457–24470.

Rincon, F., Califano, F., Schekochihin, A. A. & Valentini, F. 2016 Turbulent dynamo in a collisionless plasma. *Proc. Nat. Acc. Sci.* **113**, 3950–3953.

Rincon, F., Schekochihin, A. A. & Cowley, S. C. 2015 Non-linear mirror instability. *Mon. Not. R. Astron. Soc.* **447**, L45–L49.

Riquelme, Mario A, Quataert, Eliot & Verscharen, Daniel 2015 Particle-in-cell simulations of continuously driven mirror and ion cyclotron instabilities in high beta astrophysical and heliospheric plasmas. *Astrophys. J.* **800** (1), 27.

Riquelme, Mario A, Quataert, Eliot & Verscharen, Daniel 2016 PIC simulations of the effect of velocity space instabilities on electron viscosity and thermal conduction. *Astrophys. J.* **824** (2), 123.

Rosenbluth, M N 1956 The stability of the pinch. *Los Alamos Sci. Lab. Rep.* **LA-2030**.

Rosin, M S, Schekochihin, A A, Rincon, F & Cowley, S C 2011 A non-linear theory of the parallel firehose and gyrothermal instabilities in a weakly collisional plasma. *Mon. Not. R. Astron. Soc.* **413** (1), 7–38.

Schekochihin, A A, Cowley, S C, Dorland, W, Hammett, G W, Howes, G G, Quataert, E & Tatsuno, T 2009 Astrophysical gyrokinetics: Kinetic and fluid turbulent cascades in magnetized weakly collisional plasmas. *Astrophys. J. Supp.* **182** (1), 310.

Schekochihin, A A, Cowley, S C, Kulsrud, R M, Rosin, M S & Heinemann, T 2008 Nonlinear growth of firehose and mirror fluctuations in astrophysical plasmas. *Phys. Rev. Lett.* **100** (8), 081301.

Schekochihin, A A, Cowley, S C, Rincon, F & Rosin, M S 2010 Magnetofluid dynamics of magnetized cosmic plasma: firehose and gyrothermal instabilities. *Mon. Not. R. Astron. Soc.* **405** (1), 291–300.

Seough, Jungjoon, Yoon, Peter H. & Hwang, Junga 2015 Simulation and quasilinear theory of proton firehose instability. *Phys. Plasmas* **22** (1), 012303.

Sharma, Prateek, Hammett, Gregory W, Quataert, Eliot & Stone, James M 2006 Shearing box simulations of the MRI in a collisionless plasma. *Astrophys. J. Lett.* **637** (2), 952–967.

Sironi, L. & Narayan, R. 2015 Electron heating by the ion cyclotron instability in collisionless accretion flows. I. Compression-driven instabilities and the electron heating mechanism. *Astrophys. J.* **800**, 88, arXiv: 1411.5685.

Snyder, P B, Hammett, G W & Dorland, W 1997 Landau fluid models of collisionless magnetohydrodynamics. *Phys. Plasmas* **4** (1), 3974–3985.

Sparke, L. S. & Gallagher, III, J. S. 2007 *Galaxies in the Universe*. Cambridge University Press.

Squire, Jonathan, Quataert, E & Schekochihin, A A 2016 A stringent limit on the amplitude of Alfvénic perturbations in high-beta low-collisionality plasmas. *Astrophys. J. Lett.* **830** (2), L25.

Squire, J., Schekochihin, A. & Quataert, E. 2017 Amplitude limits and nonlinear damping of shear-Alfvén waves in high-beta low-collisionality plasmas , arXiv: 1701.03175.

Stix, T. H. 1992 *Waves in plasmas*. American Institute of Physics.

Stoneham, R. J. 1981 Nonlinear Landau damping of Alfvén waves and the production and propagation of cosmic-rays. In *Origin of Cosmic Rays* (ed. G. Setti, G. Spada & A. W. Wolfendale), *IAU Symposium*, vol. 94, p. 255.

Sturdevant, Benjamin J & Parker, Scott E 2016 Finite time step and spatial grid effects in δf simulation of warm plasmas. *J. Comp. Phys.* **305** (C), 647–663.

Told, D, Cookmeyer, J, Astfalk, P & Jenko, F 2016*a* A linear dispersion relation for the hybrid kinetic-ion/fluid-electron model of plasma physics. *New J. Phys.* **18** (7), 075001–20.

Told, D, Cookmeyer, J, Muller, F, Astfalk, P & Jenko, F 2016*b* Comparative study of gyrokinetic, hybrid-kinetic and fully kinetic wave physics for space plasmas. *New J. Phys.* **18** (6), 065011–14.

Wilkie, George J. & Dorland, William 2016 Fundamental form of the electrostatic δf-pic algorithm and discovery of a converged numerical instability. *Phys. Plasmas* **23** (5), 052111.

Yoon, Peter H., Wu, C. S. & de Assis, A. S. 1993 Effect of finite ion gyroradius on the firehose instability in a high beta plasma. *Phys. Fluids B* **5** (7), 1971–1979.

Yuan, F. & Narayan, R. 2014 Hot accretion flows around black holes. *Ann. Rev. Astron. Astro.* **52**, 529–588.

Zhuravleva, I, Churazov, E, Schekochihin, A A, Allen, S W, Arevalo, P, Fabian, A C, Forman, W R, Sanders, J S, Simionescu, A, Sunyaev, R, Vikhlinin, A & Werner, N 2014 Turbulent heating in galaxy clusters brightest in X-rays. *Nature* **515** (7525), 85–87.